RSC Advances

PAPER

View Article Online
View Journal | View Issue

Cite this: *RSC Adv.*, 2024, **14**, 33666

Magnetic self-doped TiO_{2-x}/Fe_3O_4@g-C solar-driven photocatalytic composite for water decontamination†

Nesma A. Abdel-Hady, [a] Mohamed I. Badawy,[a] Mohamed S. Attia [b] and Tarek A. Gad-Allah *[a]

Declining water resources and their contamination with chemicals risk the aquatic environment. Therefore, this work was devoted to designing a magnetically recyclable photocatalyst suitable for water treatment, namely, a TiO_{2-x}/Fe_3O_4@g-C composite. Different preparation conditions were investigated together with the corresponding characteristics. The pure defective anatase TiO_{2-x} phase of low band gap energy was detected through XRD and DRS analyses. Low charge recombination after the formation of defects was confirmed. The performances of the prepared photocatalysts in phenol degradation under solar light were evaluated, revealing the superior efficiency of TiO_{2-x} prepared hydrothermally at 200 °C/24 h relative to intact TiO_2. This best sample was incorporated with Fe_3O_4@g-C to facilitate its recovery and reuse. This successful combination was confirmed using XRD, Raman and XPS tools. TiO_{2-x}/Fe_3O_4@g-C 2 : 1 formulation was found to be the most photoactive and could be reused up to five times without significant loss in its efficiency. Therefore, the precisely developed magnetic photocatalyst is promising for application in the water-treatment process.

Received 18th August 2024
Accepted 5th October 2024

DOI: 10.1039/d4ra05990e

rsc.li/rsc-advances

1. Introduction

To date, many photocatalysts have been investigated for the degradation of different pollutants.[1] Among them, TiO_2, which was first discovered by Fujishima and Honda,[2] has attracted most of the attention owing to its excellent electronic and optical properties, electrochemical corrosion resistance, non-toxicity, good stability, low cost and abundant availability. However, the wide band-gap of TiO_2 ($E_g \approx 3.2$ eV) limits its photo-response to UV-light only, which comprises only 5% of the solar energy.[3] Numerous efforts have been devoted to improving visible light activation, including incorporating quantum dots or co-catalysts, metal deposition and doping of metals/nonmetals, and heterojunction formation with another semiconductor with an unequal band structure.[4,5,6]

Another strategy is self-doping, which can tune the electronic structures and extend the photo-response range, thereby enhancing the photocatalytic activity of semiconductors without introducing any foreign elements.[7] The improved visible light harvesting of TiO_{2-x} stems from the distortion of TiO_2 crystals *via* oxygen vacancies (OVs) or Ti^{3+}, which in turn causes the formation of new energy levels within the band gap.[8] For instance, self-doped TiO_{2-x} was prepared through the introduction of OVs in the lattice structure, leading to a narrower band-gap and enhanced visible light absorption.[8,9] TiO_{2-x} has been applied in water treatment under solar light. For instance, the TiO_{2-x}/rGO nanocomposite has been implemented in the degradation of BPA and phenol, resulting in more than 90% removal efficiency.[10] Furthermore, Wu and his co-workers[11] used Ti^{3+} self-doped TiO_2 nanoparticles as a photoanode for MB degradation and water splitting. The Ti^{3+} self-doped TiO_2 nanoparticles showed intensive light absorption, fast photogenerated carrier transport and low recombination rate, thereby exhibiting improved photocatalytic (PC) and photoelectrocatalytic (PEC) activities of the final products compared with those of pure TiO_2.

Generally, heterogeneous photocatalysts are practically applied either in an immobilized or slurry form. The immobilized form has a smaller surface area, but it is easy to be separated from water. In contrast, slurry photocatalysts have a higher surface area than immobilized ones, but they are difficult to be recovered from water. To overcome this paradox, magnetic nanoparticles can be incorporated into the powdered photocatalyst to provide an easy way to separate the photocatalyst from water using an external magnetic field without affecting the total surface area significantly.

Various methods have been employed for the synthesis of magnetic nanoparticles (MNPs) of various compositions and

[a]*Water Pollution Research Department, National Research Centre, 33 El Buhouth St., Dokki, 12622 Giza, Egypt. E-mail: tareqabdelshafy@yahoo.ca; ta.gad-allah@nrc.sci.eg; Tel: +20-33371479*

[b]*Chemistry Department, Faculty of Science, Ain Shams University, Abbassia, 11566 Cairo, Egypt*

† Electronic supplementary information (ESI) available. See DOI: https://doi.org/10.1039/d4ra05990e

phases with distinct magnetic properties. Optimal performance is achieved when the MNPs have high saturation magnetization (M_s) and stable magnetic and surface properties. Normally, MNPs possessing the strongest magnetic properties could be achieved using metals (Fe, $M_s \sim 221$ emu g^{-1})[12] or metal alloys (CoFe or CoNiFe, $M_s \sim 245$ emu g^{-1}).[13] Unfortunately, naked metal NPs have high chemical activity and are easily oxidized upon contact with air, generally leading to a loss of magnetism. This has promoted the widespread use of MNPs, such as iron(III) oxide (Fe_2O_3 and Fe_3O_4, $M_s \sim$ bulk 92 emu g^{-1}).[13] The magnetic characteristics of Fe_3O_4 nanoparticles enable their effortless recovery from water or wastewater using low magnetic fields or handheld magnets. This renders it a cost-effective and practical technique for treatment purposes owing to its benefits such as soft ferromagnetism, half-metallicity, minimal toxicity, and biocompatibility.[14]

However, high concentrations of ferrite lead to a considerable reduction in the semiconductor photocatalyst's efficiency. This is because spinel ferrites in this case act as recombination centres rather than trapping centres for electron/hole (e^-/h^+) pairs. To overcome this problem, the prepared Fe_3O_4 was covered by a barrier layer such as carbon (C) in different forms. For instance, rGO–TiO_2@Fe_3O_4 was used for the degradation of chlorophenol under visible light with efficacy equal to 94%;[15] TiO_2/Fe_3O_4/graphene oxide was investigated for the removal of methylene blue (MB) under UV light (82%) and visible light (76%);[16] on the other hand, Hatefi, Younesi *et al.* applied Fe_3O_4/TiO_2 with graphene quantum dots for the removal of MB under low-pressure mercury-vapor lamp and could achieve 86% removal efficiency.

An interesting type form of carbon is the glassy form. Glassy carbon (g-C) has high thermal resistance, extreme chemical stability, low density and great hardness compared with other carbons, which also exhibit excellent biological compatibility and high electrical conductivity.[17] The latter feature is expected to help in preventing the recombination of charge carriers, which would lead to better photocatalytic activity. Therefore, it is interesting to explore using glassy carbon as the barrier layer between self-doped TiO_2 and Fe_3O_4.

To the best of our knowledge, the TiO_{2-x}/Fe_3O_4@g-C superparamagnetic photocatalytic composite has not yet been prepared. Therefore, we devote this work to optimizing the degree of defects of TiO_{2-x} by adjusting the hydrothermal conditions used for obtaining TiO_{2-x}, thus optimizing the ratio between Fe_3O_4@g-C and TiO_{2-x} to finally have the most active and easiest magnetically separable composite. The optimization process was based on the efficiency of phenol degradation as a model organic pollutant. According to the collected results, the designed composite is very efficient under solar irradiation and can be recovered and reused successfully several times without a noticeable drop in its activity.

2. Experimental methods

2.1 Preparation of the pristine and defective TiO_{2-x}/Fe_3O_4@g-C composite

Firstly, pristine and defective TiO_2 were prepared. In typical procedure, 1.8 mL of titanium(IV) isopropoxide (TTIP, ACROS ORGANICS Co.) was added to 100 mL double distilled water (DDW) under slow stirring by a glass rod until the complete hydrolysis of TTIP. Then, the formed precipitate was washed with DDW. Subsequently, the precipitate was dissolved in 20 mL of 15% H_2O_2 aqueous solution (El-Nasr Pharmaceutical Chemical Co.). Afterward, 85 mL DDW containing 1.82 g of L-ascorbic acid (Alpha Chemika Co.) was added to prevent the formation of a dense gel. The final mixture was transferred to a 150 mL Teflon-lined autoclave and heated for different times and temperatures. The formed precipitate was collected by centrifugation at 10 000 rpm for 10 min with consecutive washings by DDW and ethanol. Finally, the powder was dried at 70 °C for 6 h under vacuum.

Fe_3O_4@g-C superparamagnetic nanoparticles were prepared as follows. Anhydrous Fe_3Cl and hexamethylenetetramine (HMTA) were dissolved in a solution of ethylene glycol and distilled water (DW) of equal volumes. The resulting solution was heated in a Teflon-lined autoclave at 110 °C for 6 h. After washing the precipitate with DW and ethanol, it was dried at 70 °C for 12 h in a vacuum oven. Then, the ground powder was calcinated at 650 °C for 1.5 h in Ar atmosphere.

Finally, the TiO_{2-x}/Fe_3O_4@g-C composites of different formulations were synthesized by suspending a definite amount of Fe_3O_4@g-C in 20 mL DDW for 15 min using an ultrasonic bath. After that, a certain amount of TiO_{2-x} was added to the Fe_3O_4@g-C suspension. The whole mixture was agitated in an ultrasonic bath for another 15 min. The well-dispersed mixture was frozen for one day, followed by freeze drying. The detailed procedure is schematically shown in Fig. 1.

2.2 Characterization of the prepared materials

Crystalline phases in the prepared materials were identified using X-ray diffraction (XRD) patterns, which were collected using an PANalytical X'Pert Pro diffractometer (the Netherlands) with CuKα source ($\lambda = 1.5406$ Å). The crystallized phases were identified by comparing the collected patterns with standard ASTM cards. The magnetization hysteresis loop was measured by a Riken Denshi BH-55 vibrating sample magnetometer (VSM) at room temperature. The band-gap was calculated from the UV-vis diffuse reflectance spectra (DRS) measured using a JASCO V730 spectrophotometer (Japan) equipped with diffuse reflectance accessories. Raman spectra were obtained using a Witec Alpha300 R confocal Raman microscope with 532 nm excitation wavelength at a power of 1 mW. The defects were identified using a BRUKER EMX EPR Spectrometer. The morphology was examined under a high-resolution transmission electron microscope (HR-TEM, JEOL TEM-2100, Japan). The recombination of electron and hole was identified using a spectrofluorometer (Edinburgh Instruments, FS5). X-ray photoelectron spectra (XPS) were collected using a Surface Science instrument X-probe, X-ray000 400 μm – FG ON.

2.3 Evaluation of the photocatalytic performance

The photocatalytic activities of the prepared materials were evaluated using phenol as a model organic pollutant under

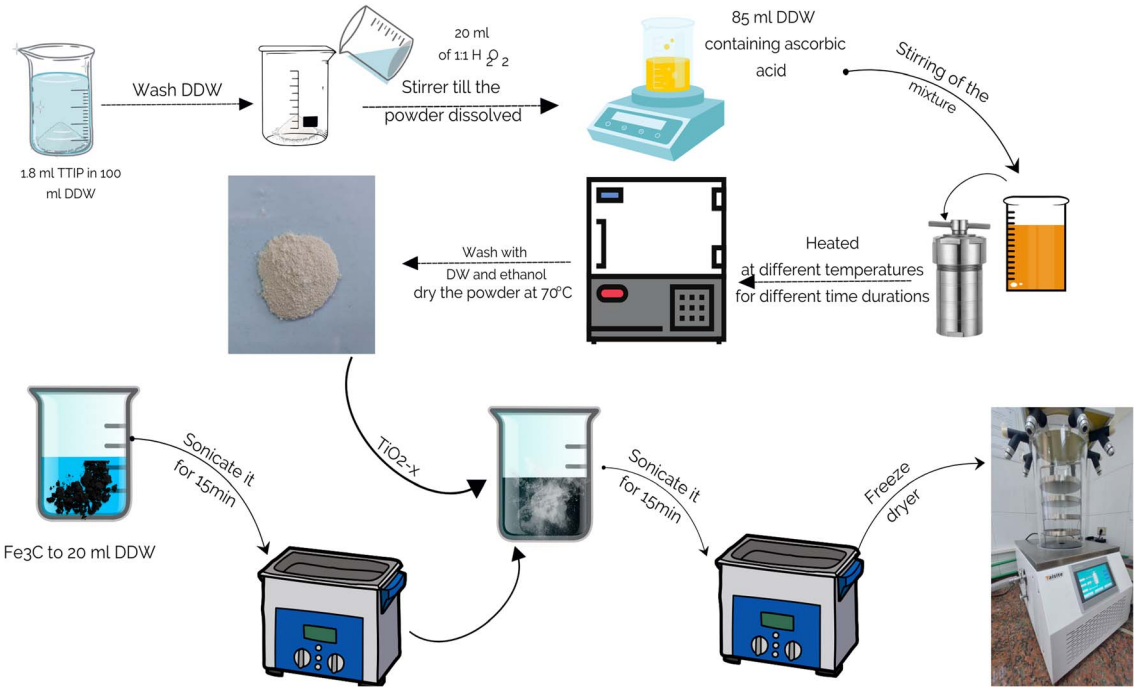

Fig. 1 Schematic preparation scheme of TiO_{2-x}/Fe_3O_4@g-C.

solar light in a batch system. A solar simulator (UVA CUBE 400, Dr Hönle AG UV Technology, Germany) equipped with a halogenide high-pressure lamp (model: SOL 500) was used for the photocatalytic experiments. This lamp emits radiation that simulates natural sunlight (1000 W m^{-2}) in a downward direction. 100 mL of phenol solution was mixed with an appropriate amount of the photocatalyst and irradiated using the solar simulator. At certain times, the samples were collected, filtered, and stored for analysis. An analogous procedure was applied for the reusability test, but the experiment was conducted for 7 h to ensure cleaning of the photocatalyst surface. Later, the photocatalyst was collected using an external magnetic field. The collected powder was washed with DW and ethanol before using in the next experiment.

Phenol concentrations were analysed using a high-performance liquid chromatograph (HPLC, Agilent 1260, USA) based on the following conditions: 60 : 40 water and acetonitrile as isocratic eluent, 25 °C column temperature, and detection at 280 nm wavelength.

3. Results and discussion

3.1 Optimization of the pure photocatalyst

3.1.1. Characteristics of the pristine and defective TiO_2. X-ray diffraction (XRD) was used to investigate the effect of

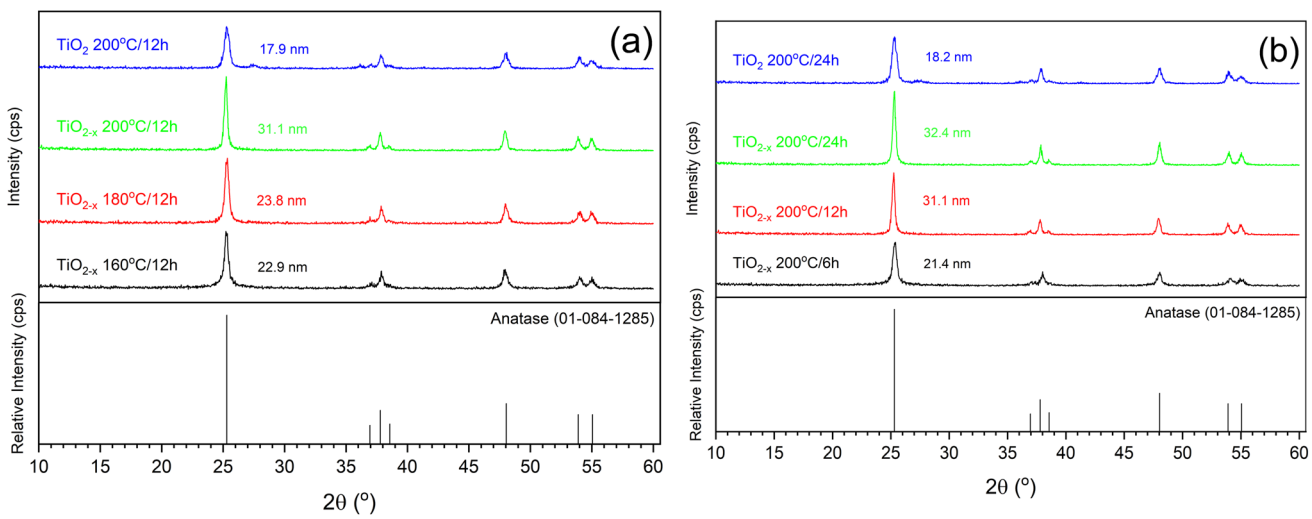

Fig. 2 XRD patterns of pure and defective TiO_2 samples prepared at different (a) temperatures and (b) times.

hydrothermal conditions on the crystal structure of the as-prepared samples, as presented in Fig. 2. Generally, all the prepared materials exhibited diffraction peaks matching the (101), (103), (004), (112), (200), (105), (211) planes of anatase TiO_2 (ICDD no. 01-084-1285), without any additional diffraction peaks related to other phases, thus indicating the high purity of the prepared samples. According to the data in Fig. 2a, increasing the hydrothermal temperature resulted in an enhanced crystallinity of TiO_{2-x}, as evidenced by the increasing peaks intensities and decreasing full-width half maxima of the peaks. Thus, 200 °C was chosen as the optimum temperature and was utilized to study the effect of the hydrothermal time. The patterns in Fig. 2b illustrate the growth of TiO_{2-x} crystals with the time of the hydrothermal process. On comparing the crystallite sizes calculated using Scherrer equation,[18] it was found that both time and temperature of the hydrothermal process have a similar effect on the crystallinity of the produced material. The effect of ascorbic acid on the crystallinity could be explored by comparing the XRD patterns of the samples prepared in the presence or absence of ascorbic acid under the same hydrothermal conditions (*i.e.*, pristine and defective TiO_{2-x}). The addition of ascorbic acid enhanced the crystal size. Therefore, it can be deduced that the addition of ascorbic acid led to the formation of large defected crystals, as shown in TEM images. The same phenomenon was previously reported in the defective TiO_2 prepared using the same reducing agent.[19,20] It is worth mentioning that the hydrothermal time did not significantly affect the crystallinity of the pristine TiO_2 samples prepared in 12 h and 24 h (17.9 and 18.2 nm, respectively). This further highlights the effect of ascorbic acid on the crystallinity of titania crystals under different hydrothermal conditions.

The UV-vis diffuse reflectance (DRS) technique was used to evaluate the optical properties of the prepared samples. The absorption coefficients were calculated from the DRS spectra using the Kubelka–Munk equation,[21] $\alpha = K/S = (1 - R)^2/2R$, where K is the absorption coefficient, S is the scattering

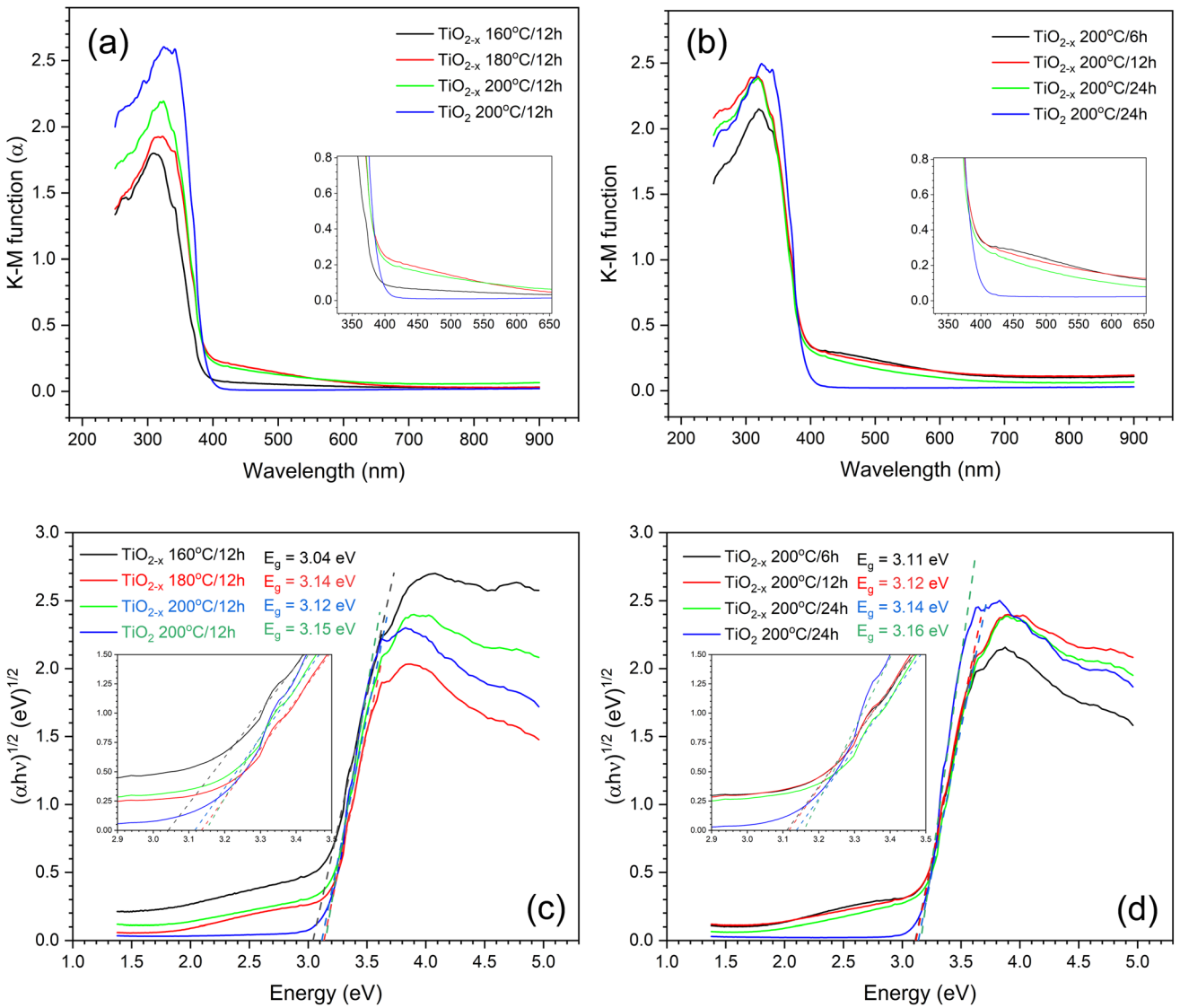

Fig. 3 (a and b) Transformations of the UV-vis DRS spectra, and (c and d) Tauc plot of TiO_2 prepared under different hydrothermal conditions.

coefficient, and R is the reflectance obtained from DRS. The calculated spectra are shown in Fig. 3a and b. Increasing the hydrothermal reaction time caused an increase in the absorptivity of the prepared samples either in UV or visible light range, which may be due to either the enhanced crystallinity of the samples, as previously observed by the XRD results, or the formation of more defects. Unfortunately, it was difficult to segregate the effects of grain size and self-doping under the studied conditions. The same obstacles were previously reported.[22] However, comparing the TiO_2 and TiO_{2-x} prepared under the same conditions (*i.e.*, 200 °C/12 h) revealed that TiO_{2-x} exhibited better absorption in the visible light range, which can be due to the presence of defects that form a shallow donor level below the conduction band, thus narrowing the band gap.[22] This level originates from the Ti dangling bonds associated with the shortage of oxygen atoms.[23] Since TiO_{2-x} (200 °C) displayed the best absorption in both UV and visible light ranges, it was used to assess the variation in DRS with the hydrothermal time at this temperature, as shown in Fig. 3b. It is evident that the absorption of TiO_{2-x} samples slightly decreases with increasing time of hydrothermal treatment; nevertheless, all TiO_{2-x} still possess better absorption in the visible light region than the TiO_2 sample. The Tauc plots presented in Fig. 3c and d support the shrinkage in the band-gap when using ascorbic acid under the investigated conditions. However, the calculated band-gaps do not follow the same order observed in the absorption spectra. This might be due to the incorrectness of the band-gap calculation using Tauc plots in the case of doped semiconductors, as previously reported.[21] To sum up, temperature plays a major role in governing the optical properties of the defective TiO_{2-x} rather than the time of the hydrothermal process.

PL spectra were measured to assess the recombination of the photogenerated electron–hole pairs. A lower fluorescence intensity implies the limited recombination of electrons and holes, which is beneficial to the photocatalytic performance because of the high number of free charges available for the photocatalytic reaction.[24] Fig. S1† shows the recorded PL spectra of TiO_2 and TiO_{2-x} prepared under different hydrothermal conditions. Samples prepared using ascorbic acid (*i.e.*, TiO_{2-x}) at any of the studied hydrothermal temperatures showed quenched PL intensities, as illustrated in Fig. S1a.† Specifically, TiO_{2-x} 200 °C/12 h showed the lowest PL intensity, indicating that this sample possesses the lowest charge recombination and possibly the best photocatalytic performance. The study of the effect of hydrothermal time, presented in Fig. S1b,† shows that short hydrothermal time led to low PL intensity, while a longer time (*i.e.*, 24 h) resulted in a slightly higher PL intensity. However, it should be mentioned that the pristine TiO_2, prepared in the absence of ascorbic acid, still possesses the highest PL intensity, indicating the formation of new sublevels in the samples prepared using ascorbic acid due to the formed defects. Therefore, it can be deduced that although ascorbic acid enhanced the growth of TiO_2 crystals, according to the XRD results, it caused a deformation of the formed crystals, as evidenced by the low PL intensities of the samples prepared in the presence of ascorbic acid.

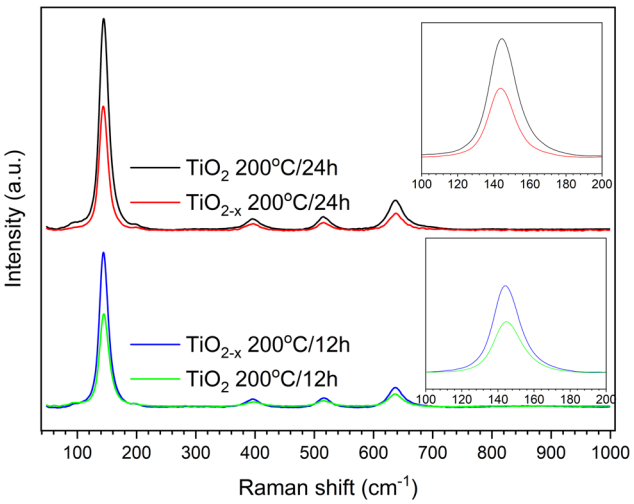

Fig. 4 Raman spectra of TiO_2 and TiO_{2-x} prepared at 200 °C in 12 h and 24 h.

Another important analytical tool to determine the crystalline phases and any defects in them is Raman spectroscopy. As shown in Fig. 4, similar peaks appearing at 144 cm^{-1}, 396 cm^{-1}, 516 cm^{-1} and 636 cm^{-1} were observed in all the samples. These peaks can be assigned specifically to the E_g, B_{1g}, A_{1g}, and E_g vibrational modes in the anatase TiO_2 crystal, as reported out by Wang *et al.*,[25] indicating the good purity of the prepared samples. This is consistent with the XRD results shown above. A deep investigation of the Raman spectra of the TiO_{2-x} samples indicated a lower peak intensity with a small shift toward a lower wavenumber relative to the pristine TiO_2 sample that was hydrothermally treated for 24 h (insets of Fig. 4). This refers to the presence of surface disorder, as reported by Gu, Pan *et al.*,[26] enclosing localized defects that originated from the formation of Ti^{3+} (ref. 27) or oxygen vacancies (*i.e.*, Ti–Ov–Ti bonds).[28] On the contrary, the peaks of pristine TiO_2 prepared in 12 h appeared at almost the same position as those of the corresponding defected sample TiO_{2-x} but with higher intensities. This shows that ascorbic acid enhanced the crystallization in a shorter time of hydrothermal treatment rather than the formation of defects in the growing crystals. This speculation is also supported by the measured crystallite sizes shown in Fig. 2 (*i.e.*, 31.1 nm and 17.9 nm for TiO_{2-x} 200 °C/12 h and TiO_2 200 °C/12 h, respectively). Therefore, it can be deduced that the role of ascorbic acid varies according to the hydrothermal time; it mainly supports the crystal growth during a short hydrothermal time, then deforms the formed crystals on increasing the hydrothermal time.

In order to support the previous speculation, the morphology of TiO_2 200 °C/12 h, TiO_2 200 °C/24 h, TiO_{2-x} 200 °C/12 h and TiO_{2-x} 200 °C/24 h was imaged under TEM, as shown in Fig. 5. Generally, all samples are composed of nanoparticles (*i.e.*, particle size < 100 nm). For short hydrothermal time, TiO_2 200 °C/12 h shows mostly ~22 nm cuboid particles, as depicted in Fig. 5a. However, the TEM image for TiO_{2-x} 200 °C/12 h in Fig. 5b illustrated that adding ascorbic acid deformed the crystals during their growth, leading to the formation of

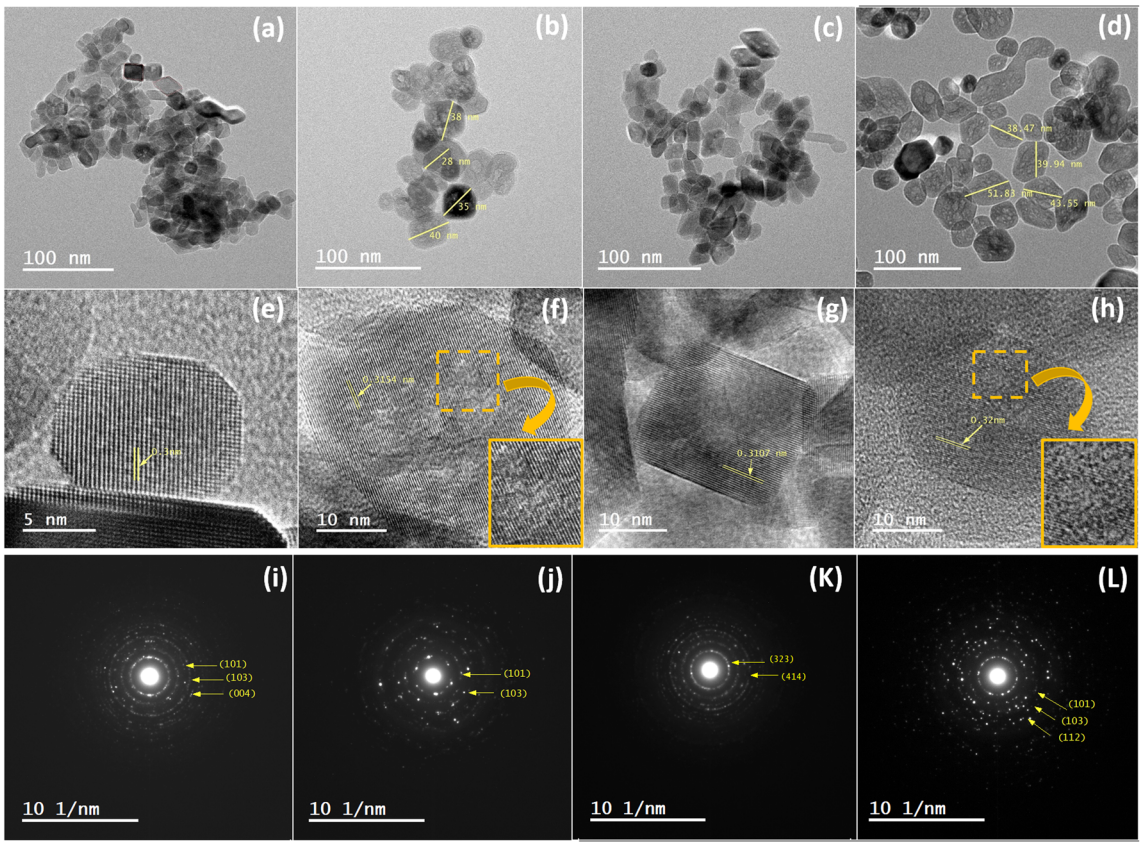

Fig. 5 TEM images of TiO_2 and TiO_{2-x} samples: (a, e and i) TiO_2 200 °C/12 h, (b, f and j) TiO_{2-x} 200 °C/12 h, (c, g and k) TiO_2 200 °C/24 h and (d, h and l) TiO_{2-x} 200 °C/24 h.

irregular nanoparticles. Furthermore, ascorbic acid increased the particle size to ~35 nm, which is nearly 1.6 times that of the pristine TiO_2 200 °C/12 h sample. The TiO_2 200 °C/24 h sample prepared at a longer hydrothermal time (24 h) constitutes a well-defined cuboid of 22 nm size, which is nearly the same as TiO_2 200 °C/12 h (Fig. 5c). This observation is in line with the XRD analyses shown in Fig. 2. The TEM image of the TiO_{2-x} 200 °C/24 h sample in Fig. 5d also shows a larger deformed nanoparticle, with an average size of ~44 nm, than its control sample (*i.e.*, TiO_2 200 °C/24 h) and the defected sample prepared at a shorter hydrothermal time (*i.e.*, TiO_{2-x} 200 °C/12 h). The increase in the particle size may be due to the ascorbic acid

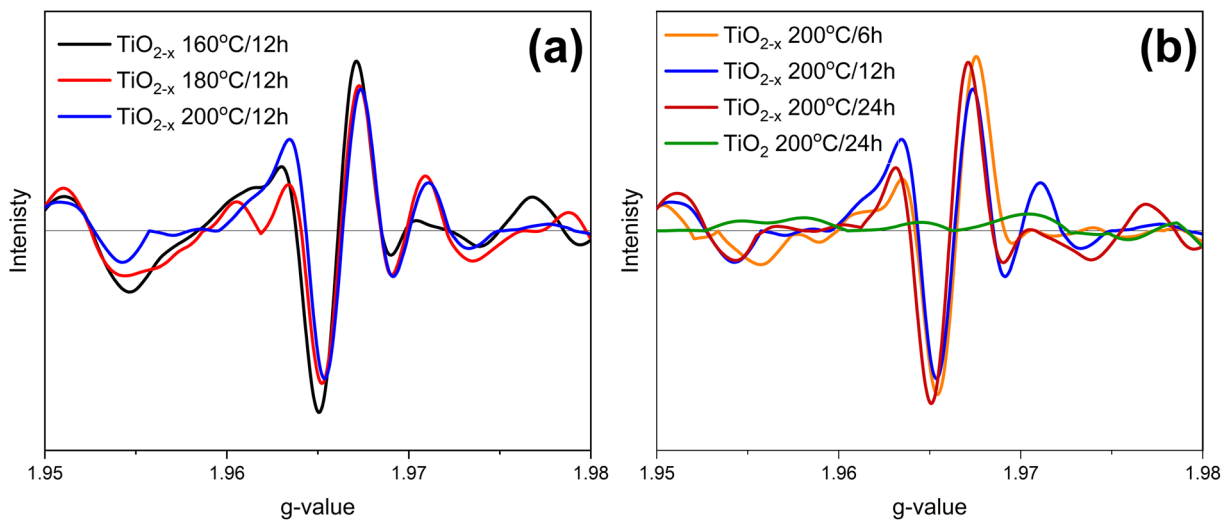

Fig. 6 EPR spectra of the prepared samples; effects of (a) temperature and (b) time.

effect and elongated hydrothermal time. It is worth mentioning that the measured particle sizes are consistent with the sizes calculated from the XRD patterns.

Fig. 5e–h shows the lattice spacing of TiO_2 200 °C/12 h, TiO_{2-x} 200 °C/12 h, TiO_2 200 °C/24 h, and TiO_{2-x} 200 °C/24 h samples with values of 0.3, 0.315, 0.3107 and 0.32 nm, respectively, corresponding to the interplanar crystal spacing of the (101) plane. Generally, the selected area electron diffractions of the whole samples show strong dotted-rings diffraction pattern, referring to the polycrystalline nature of these samples. The identified planes from the SAED pattern were (101), (103) and (004) in case of TiO_2 200 °C/12 h, (101) and (103) in case of TiO_{2-x} 200 °C/12 h, (101) and (112) in case of TiO_2 200 °C/24 h, and (101), (103) and (112) in case of TiO_{2-x} 200 °C/24 h. All of these planes are characteristic for the anatase crystals, indicating the high purity of the prepared samples.

EPR spectroscopy was used to identify the defect type, *i.e.*, Ti^{3+} or oxygen vacancies, in the prepared samples. The collected EPR spectra are elucidated in Fig. 6. TiO_2 200 °C/24 h shows an insignificant EPR signal due to the diamagnetic nature of TiO_2. On the other hand, all the prepared samples exhibited a strong signal at g ~1.966, revealing the presence of Ti^{3+}, as previously reported by Zhang *et al.*[29] However, it was difficult to determine which sample has more defects because the differences in the signal intensities are insignificant. Therefore, it can be concluded that Ti^{3+} is the major defect caused by ascorbic acid. This result is consistent with the previously reported research.[30]

XPS technique was used to shed light on the components, chemical states of the elements, and nature of the defects in the prepared materials. The high-resolution XPS spectra of the detected elements are presented in Fig. 7. According to the full-scan data presented in Fig. 7a, three elements, namely, carbon,

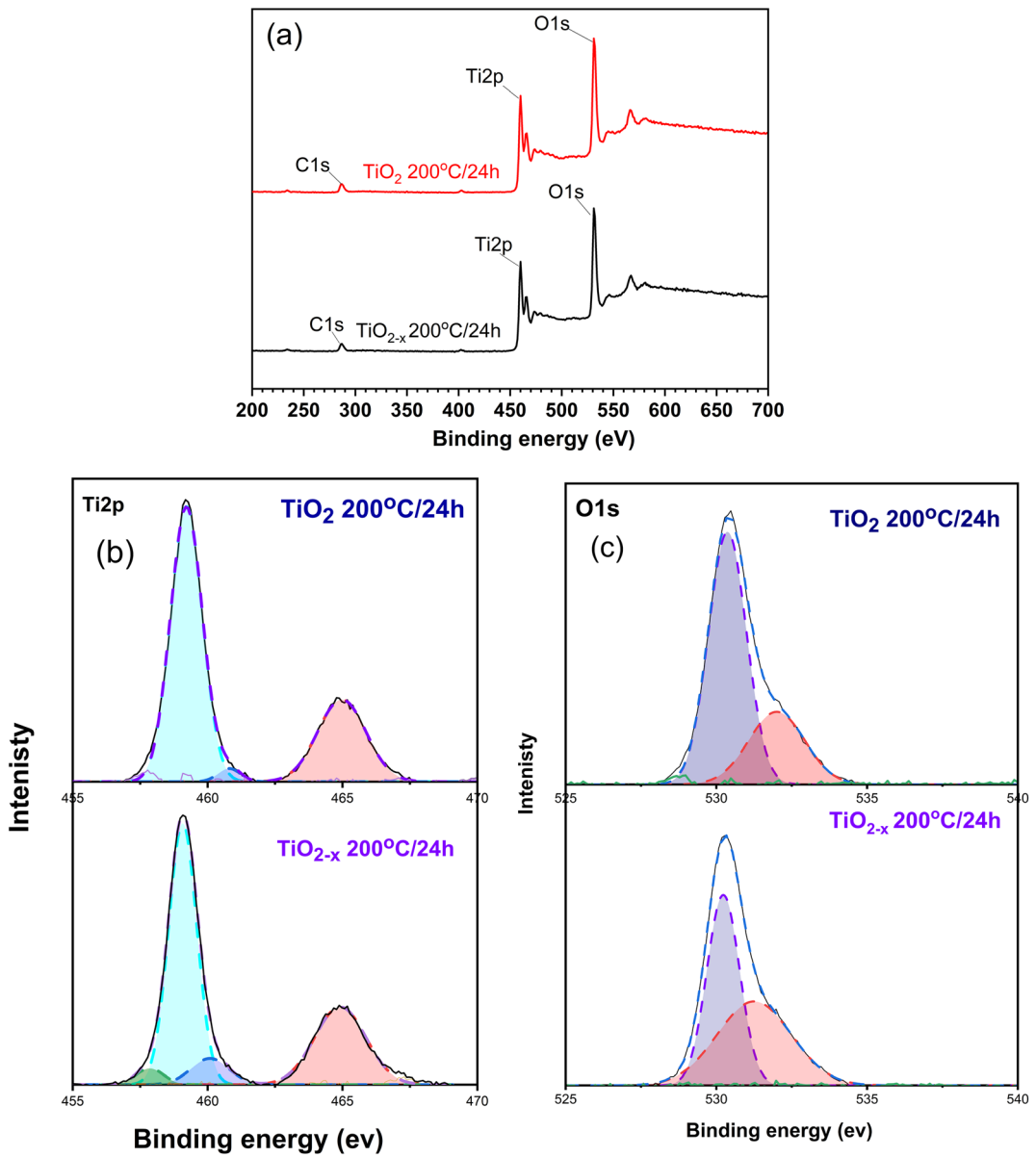

Fig. 7 XPS spectra of the prepared samples; (a) full scan and (b and c) deconvoluted spectra of Ti and O elements.

oxygen, and titanium, could be recognized in the spectra of all the samples. The peak of carbon (*i.e.*, C 1s) at 284.6 eV is probably due to the contamination by atmospheric carbon during sample preparation.[31]

Fig. 7b displays the Ti 2p peaks of the intact and defective TiO_2 prepared at 200 °C for 24 h under the hydrothermal conditions. The intact sample (*i.e.*, TiO_2) showed two peaks at 459.19 and 464.89 eV corresponding to the Ti^{4+} $2p_{3/2}$ and Ti^{4+} $2p_{1/2}$ states, respectively.[32] These peaks were shifted to lower binding energies in the defective sample (TiO_{2-x}), *i.e.*, 459.09 and 464.74 eV, respectively. This suggests the formation of Ti^{3+} defects in this sample. Deconvoluting the two major peaks revealed the presence of a peak at 460.8 eV corresponding to Ti^{3+} in Ti_2O_3. This indicates that both TiO_2 and Ti_2O_3 are formed in the prepared samples but with different intensities; in TiO_{2-x} 200 °C/24 h, the peak intensity is more than TiO_2 200 °C/24 h by 4 times, indicating the presence of more defects. Deconvoluting the peak at 459.09 eV in case of the TiO_{2-x} 200 °C/24 h sample showed a new peak at 457.7 eV, which confirms the formation of Ti^{3+}.[33]

The high resolution XPS spectrum of O 1s in Fig. 7c depicts two peaks centred at 530.36 and 531.2 eV for the TiO_2 200 °C/24 h sample. These peaks are representative for the Ti–O–Ti and surface –OH species, respectively, as previously reported.[34] On the other hand, the shift of the peak at 530.2 eV in TiO_{2-x} 200 °C/24 h originates from the formation of the oxygen vacancy near the Ti^{3+}, according to ref. 32. Furthermore, the increase in the peak at 531.2 eV indicates the formation of oxygen vacancy, as mentioned by ref. 35.

3.1.2. Performance of the pristine and defective TiO_2. In the beginning, the photocatalytic performances of the pure pristine and defective TiO_2 (TiO_{2-x}) prepared under different hydrothermal conditions (temperature = 160, 180, and 200 °C; time = 6, 12, and 24 h) were assessed in terms of the removal of phenol under solar light. Generally, the non-linear fitting of the collected data, with the coefficient of determination (R^2) ranging from 0.884 to 0.998 and chi-square (χ^2) values between 1.53×10^{-4} and 1.18×10^{-2}, revealed good adherence to the first-order kinetics, as shown in Fig. 8a. The calculated first-order rate constants for each material were compared in Fig. 8b in order to assess the effect of preparation conditions on the photocatalytic process. It has been shown that increasing the hydrothermal time enhanced the activity in general. Similarly, the increased hydrothermal temperature had a positive effect on the photocatalytic activity. These observations are in line with the enhanced crystallinity and optical properties, as referred previously. Interestingly, the defected TiO_{2-x} showed a significantly improved photocatalytic activity relative to pristine TiO_2 because it consists of large deformed particles, which resulted in better charge separation, as evidenced by TEM and PL analyses shown above. Based on the findings in Fig. 8b, it is evident that the degradation rate of phenol is higher using TiO_{2-x} 200 °C/24 h compared to TiO_{2-x} 200 °C/12 h. This might be attributed to the formation of massive defects in TiO_{2-x} 200 °C/12 h,[36] which might hinder the formation of a reasonable number of charge carriers. On the other hand, when it comes to TiO_{2-x} 200 °C/24 h, the increase in the hydrothermal time helped in the formation of larger crystal size, which played a crucial role in the enhanced degradation of phenol.

3.2 Optimization of the magnetic composite

3.2.1. Characteristics of the magnetic composite. Based on the characteristics and performance of the pristine and defective TiO_2, it was obvious that the TiO_{2-x} sample prepared under the hydrothermal conditions at 200 °C/24 h exhibits the best performance. Thus, it was decided to merge this sample in different ratios with the magnetic component Fe_3O_4. The XRD patterns of the pure magnetic component and the prepared composites are illustrated in Fig. S2.† The pure magnetic component pattern shows diffraction peaks at 2θ = 30.31°, 35.6°, 43.3°, 53.7° and 57.13°, which can be ascribed to the (311), (220), (400), (422), and (511) diffraction planes, respectively, for the magnetite (Fe_3O_4) phase (ICDD no. 01-088-0315).

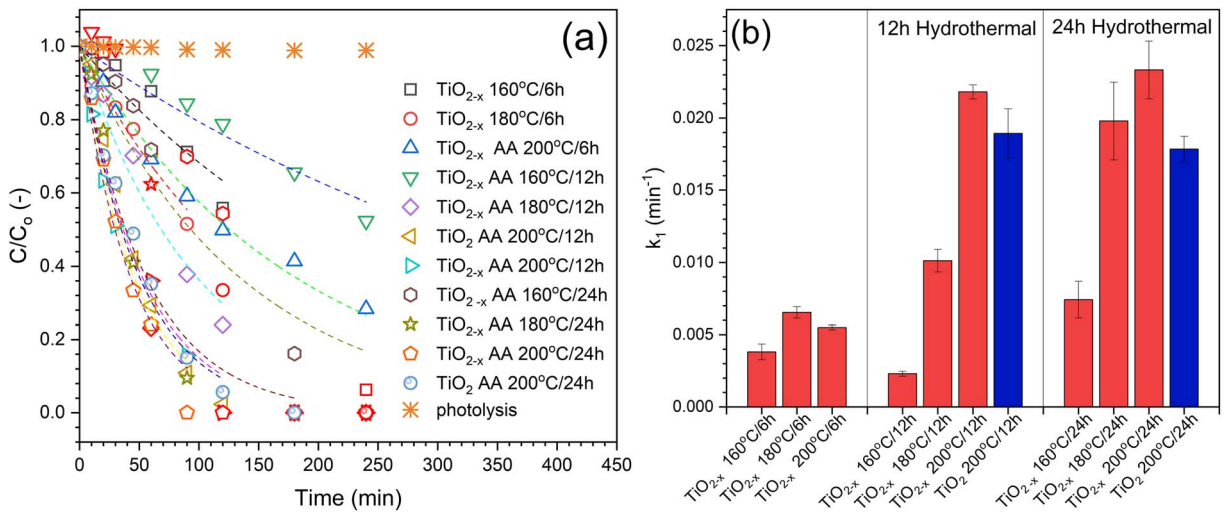

Fig. 8 Photocatalytic degradation of phenol using pristine and defective TiO_2 prepared at different hydrothermal conditions. (a) Experimental data with 1st order kinetics fitting, and (b) comparison of the calculated rate constants [100 mg per L catalyst, 10 mg per L phenol, and natural pH].

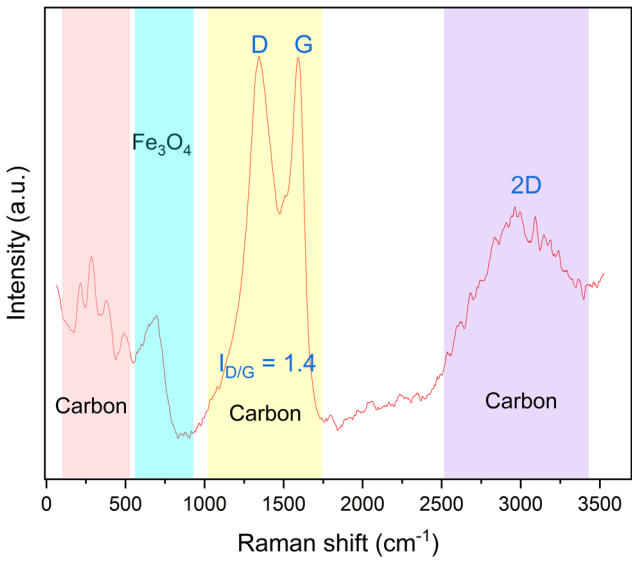

Fig. 9 Raman spectra of the prepared magnetic component.

All the composite samples displayed the peaks of the Fe_3O_4 phase along with the peaks relevant to the TiO_2 anatase phase (ICDD no. 01-084-1285). This suggests the successful formation of the magnetic photoactive composites. It is worth mentioning that the difference in the peak intensities between Fe_3O_4 and TiO_2 were varied according to the mixing ratio between the two components. This is another evidence of the effective binding between the two components because magnetic recovery was done during the washing of the prepared composites.

Although XRD analysis suggested the formation of the Fe_3O_4 phase, it is possible to have maghemite (Fe_2O_3) also in our sample since the two phases, *i.e.*, Fe_3O_4 and Fe_2O_3, possess superimposed XRD peaks. Raman spectroscopy has been widely used to differentiate the iron oxides, especially magnetite and maghemite. The representative Raman spectrum of the synthesized magnetic material is presented in Fig. 9. The broadband at 688 cm^{-1} can be assigned to the A_{1g} transition of magnetite.[37] According to Chen *et al.*,[38] the two strong peaks at 1345 cm^{-1} and 1593 cm^{-1} refer to the D and G modes of graphitic carbon, respectively, and the ratio between the area under the peak of those peaks (*i.e.*, $I_{D/G}$) is used as a measurement of the relative degree of disorder in the carbonaceous materials. $I_{D/G}$ was found to be 1.4, which is higher than unity, indicating the presence of a substantial graphitization degree and a high sp^2 content in the formed carbon.[17,39] Moreover, there are low frequency bands in the range of 200–500 cm^{-1}, which correspond to P1, P2, P3 and P4, whose peaks appear in case of glassy carbon, as mentioned by Jurkiewicz and co-workers.[17] Additionally, there is an overtone broad peak at 2500–3450 cm^{-1}. The deconvolution of this peak showed two bands at approximately 2670 cm^{-1} and 3000 cm^{-1} corresponding to the 2D bands in glassy carbon.[40] To sum up, the magnetic component prepared in this study consists of Fe_3O_4 with glassy carbon.

The morphology of the pure magnetic component and the prepared composites were visualized in the TEM images depicted in Fig. 10. From Fig. 10a, it can be seen that the magnetic component is composed of irregular nanoparticles with an average size of ~13.5 nm, covered with a glassy carbon sheet. The lattice spacing of the observed nanoparticles is 1.859 nm, which is corresponding to the interplanar crystal spacing of the (331) plane of Fe_3O_4. These observations demonstrate that the prepared magnetic component is Fe_3O_4@g-C. The inset selected area electron diffraction (SAED) image shows blurry dotted rings, indicating the polycrystalline nature of this samples. The successful formation of the TiO_{2-x}/Fe_3O_4@g-C composite was confirmed according to the images in Fig. 10b and c. In these images, both Fe_3O_4@g-C and TiO_{2-x} crystals could be clearly recognized, and their abundance is relatively consistent with the added amounts. Furthermore, the inset images of SAED in Fig. 10b and c belonging to the TiO_{2-x} crystals showed very strong diffraction patterns due to the good crystallinity of TiO_{2-x}, unlike the vague SAED of Fe_3O_4@g-C. This disparity arises from the carbon cover on Fe_3O_4, whereas the TiO_{2-x} crystals are naked.

The magnetic properties of the prepared materials were assessed using VSM analysis, as shown in Fig. 11. The Fe_3O_4@g-C sample showed the desired superparamagnetic behaviour, *i.e.*, of 55 emu g^{-1} magnetization saturation (M_s) with low

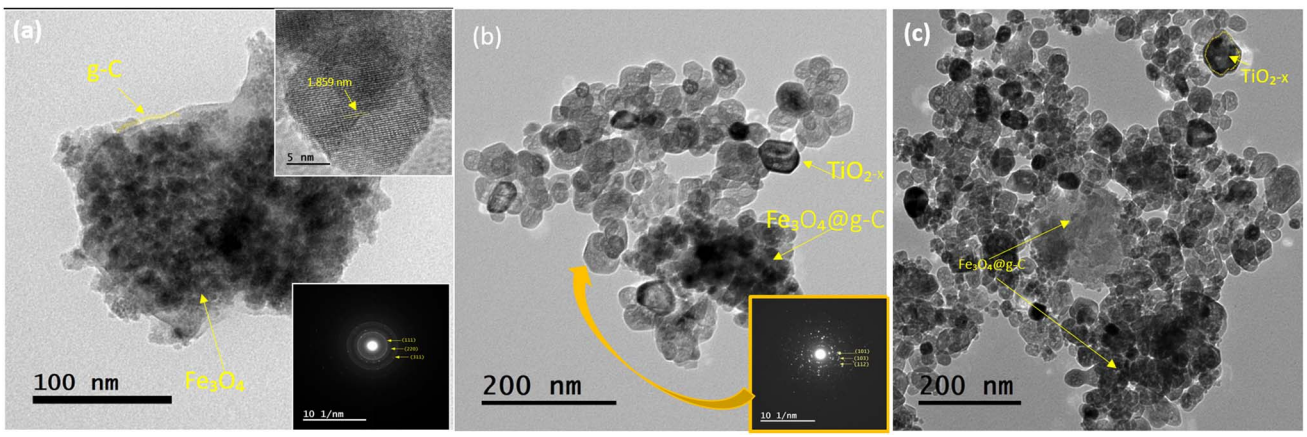

Fig. 10 TEM images of (a) Fe_3O_4@g-C and (b) TiO_{2-x}/Fe_3O_4@g-C 200 °C/24 h 1 : 1 and (c) TiO_{2-x}/Fe_3O_4@g-C 200 °C/24 h 4 : 1.

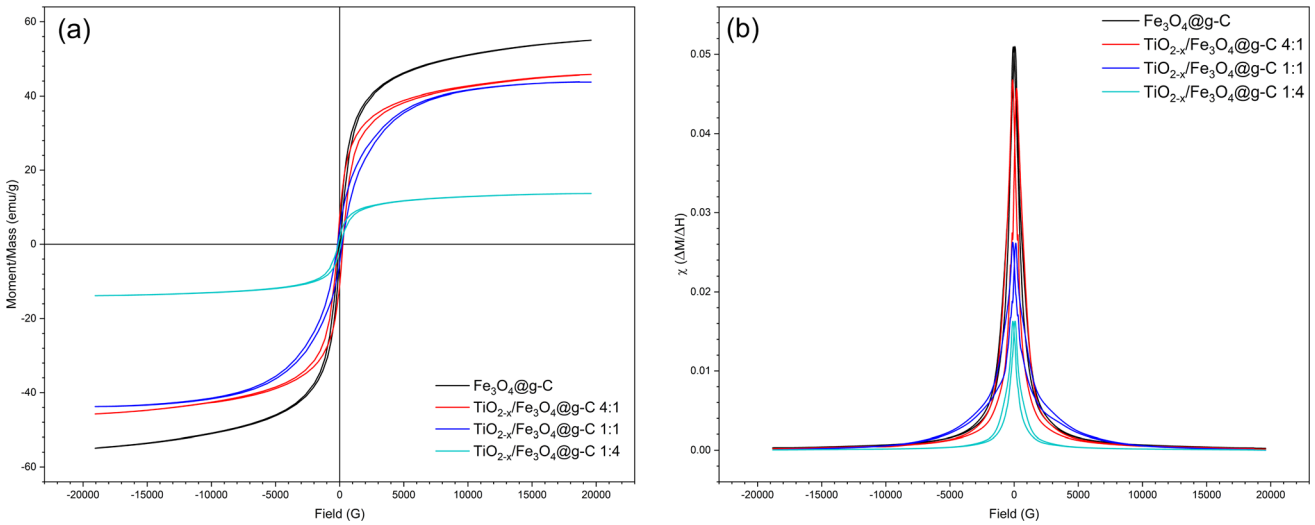

Fig. 11 (a) VSM hysteresis loops and (b) magnetic susceptibility of the pure Fe_3O_4@g-C and TiO_{2-x}/Fe_3O_4@g-C composite of different ratios.

coercivity (H_c) and retentivity (M_r) (Fig. 11a). As expected, the sample with more Fe_3O_4@g-C content showed high saturation magnetization (M_s), whereas the samples containing more TiO_{2-x} content showed low saturation magnetization (M_s). However, all the samples possess superparamagnetic behaviour, enabling fast magnetization under the effect of an external magnetic field and good dispersion in its absence.

Another evidence of the good magnetic behaviours of the prepared samples were deduced from their magnetic susceptibility (χ), as shown in Fig. 11b, since χ is a measure of the response of a material to an applied magnetic field. The calculated χ values for the prepared samples fall within the range $>10^{-2}$ to $\sim 10^{5}$, which is characteristic of superparamagnetic materials, as reported by Frenea-Robin and Marchalot (2022).[41] As shown in Fig. 11b, the TiO_{2-x}/Fe_3O_4@g-C 4 : 1 sample exhibited χ close to that of Fe_3O_4@g-C due to the high content of Fe_3O_4 in this sample. Though the higher TiO_{2-x} content (four times) decreases the χ value because of the increasing amount of non-magnetic component in the composite, this sample exhibits good susceptibility to an external magnetic field. To sum up, the prepared composites showed excellent magnetic properties, qualifying their application as magnetically recoverable photocatalysts.

The chemical composition and binding energies of the TiO_{2-x}/Fe_3O_4@g-C composite was examined by XPS. Full scan revealed the presence of Fe, O, Ti and C elements in this sample, as evidenced by the appearance of peaks at 713.26, 531.83, 460.09 and 286.5 eV corresponding to the Fe 2p, O 1s, Ti 2p, and C 1s energy states, respectively, as shown in Fig. 12a.

In the Ti 2p spectra illustrated in Fig. 12b, the sample revealed two peaks of Ti^{4+} $2p_{3/2}$ and Ti^{4+} $2p_{1/2}$ at 459.22 and 464.81 eV, respectively. As discussed above in the corresponding pure TiO_{2-x} sample, the Ti 2p peaks shifted to a lower binding energy relative to the pristine TiO_2, demonstrating the formation of Ti^{3+} ions. The deconvolution of the peak at 459.22 eV demonstrated a peak at 457.7 eV, which further confirms the presence of the Ti^{3+} defect. The peak at 460 eV is also an indication of Ti^{3+}. The increase in this peak intensity compared to TiO_{2-x} is attributed to the formation of new bonds between Fe–O–Ti and Ti–O–C.[32] Thereby, the method used for synthesising the magnetic composite, *i.e.*, Fe_3O_4@g-C/TiO_{2-x}, did not affect the defect in the TiO_2 crystals, and it is expected not to affect the photocatalytic activity.

The O 1s spectrum in Fig. 12c resulted in three peaks: the broad band centred at 530.28 eV that can be assigned to Ti–O, Fe–O and Fe–O–Ti bonds,[42] the peak at 533.29 eV can be attributed to the surface C–O bond,[43] and the peak at 531 eV is due to the formation of Fe–O–C.[43] The formation of Fe–O–C bonds is evidence of the strong binding between Fe_3O_4@g-C and TiO_{2-x} in the composite, which guarantee the stability of the composite during the treatment and reuse processes.

Fig. 12d depicts the characteristic peaks of Fe 2p at 711.03 and 724.13 eV, which can be assigned to the spin–orbit peaks of Fe $2p_{3/2}$ and Fe $2p_{1/2}$, which is in good agreement with the previously published literature.[42] Two satellite signals of the Fe $2p_{3/2}$ and Fe $2p_{1/2}$ peaks were observed at the same time, which can be attributed to the oxidation states of Fe^{3+} and Fe^{2+} in Fe_3O_4 nanoparticles.[44]

The high-resolution C 1s spectrum in Fig. 12e was deconvoluted into four peaks. The peaks at 284.8 and 286.1 eV can be ascribed to C=C and C–C, respectively, which is an indication of the graphitic structure of glassy carbon, and the peak at 290 eV is ascribed to the presence of the carboxylate carbon.[39] There is another peak at 289.1 eV, which is due to the formation of the Ti–O–C bond.[45] The formation of the Ti–O–C bond is another evidence of the strong linkage inside the composite TiO_{2-x}/Fe_3O_4@g-C.

3.3 Performance of TiO_{2-x}/Fe_3O_4@g-C

The different composite formulations were investigated for the photocatalytic degradation of phenol in order to determine the

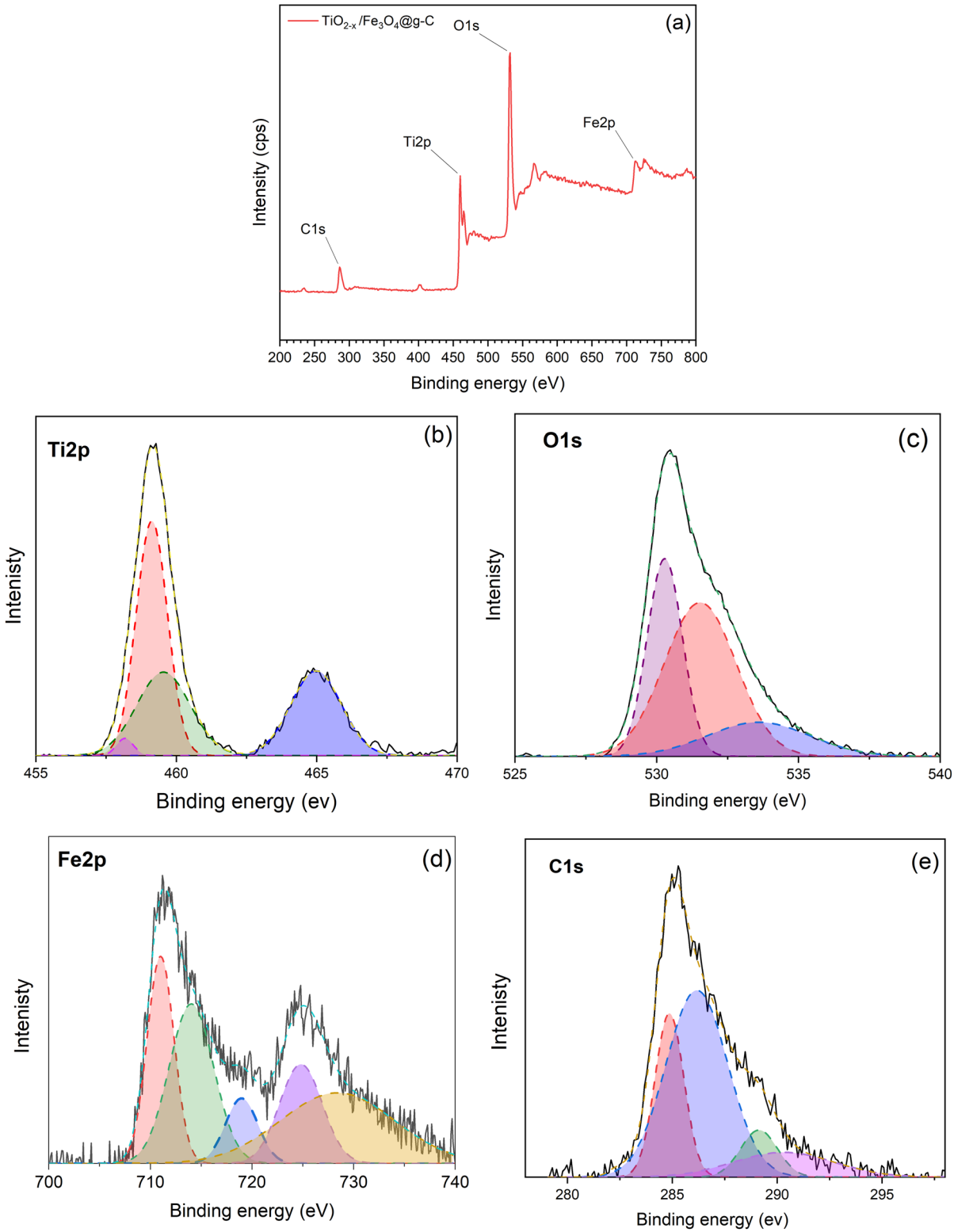

Fig. 12 XPS spectra of the TiO_{2-x}/Fe_3O_4@g-C 1 : 1 composite; (a) full scan spectrum, (b) Ti 2p, (c) O 1s, (d) Fe 2p and (e) C 1s spectra.

best formulation. The time-dependent photocatalytic data is illustrated in Fig. 13a. Generally, the photocatalytic processes using the prepared samples followed the first-order kinetics. However, these observations are not accurate because the prepared composites contain different amounts of the photoactive component, *i.e.*, TiO_{2-x}. Therefore, the TiO_{2-x} content in each composite sample was determined using the ICP technique (Fig. 13c) in order to calculate the activity precisely. There

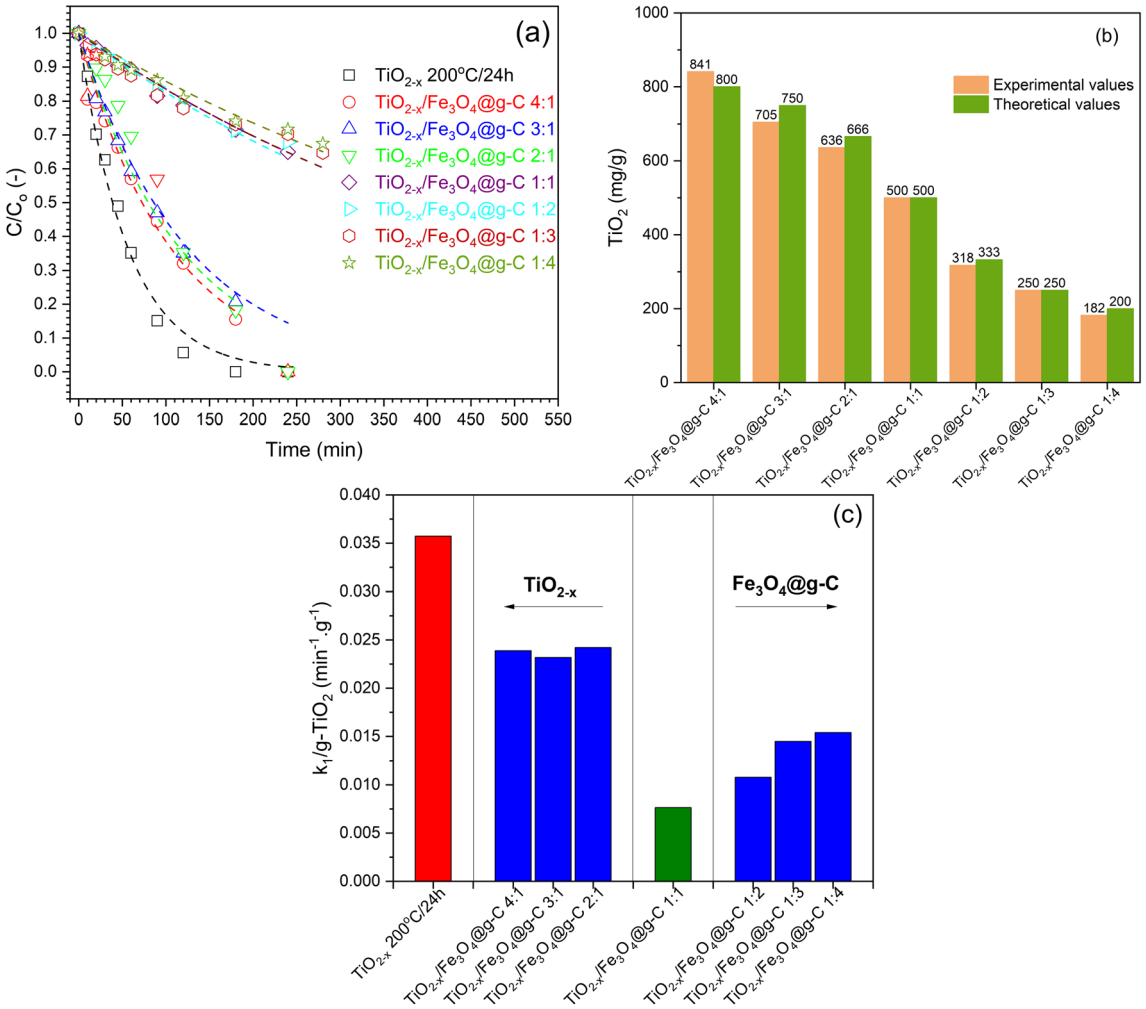

Fig. 13 (a) Experimental data of phenol photocatalytic degradation with 1st order kinetics fitting, (b) ICP analysis of TiO_2 content in the prepared samples, (c) corrected rate constants based on the TiO_2 content.

was no significant difference between the experimental and calculated values of the TiO_{2-x} amount, indicating the efficiency of the method used to obtain the TiO_{2-x}:Fe_3O_4@g-C composite. After correcting the obtained k_1 values based on the TiO_{2-x} amount in each sample, the calculated first-order rate constants (k_1) are compared in Fig. 13c to compare the activities of the prepared samples. It has been realized that the higher ratio of TiO_{2-x} led to better activity, which is more logical due to the addition of more photoactive sites to the system. In addition, the higher ratio of TiO_{2-x} allowed the contact of TiO_{2-x} with the glassy carbon in Fe_3O_4@g-C, which is responsible for the efficient separation of the photo-generated charges in TiO_{2-x}, as previously reported.[17] On the contrary, increasing the TiO_{2-x}:Fe_3O_4@g-C more than 1:1 did not enhance the photocatalytic process because the excess Fe_3O_4@g-C will not be in contact with TiO_{2-x}. Therefore, the TiO_{2-x}:Fe_3O_4@g-C composites of 1:2 and 4:1 ratios are the formulations that result in the best photocatalytic activity.

Phenol photodegradation using TiO_{2-x}/Fe_3O_4@g-C as the catalyst is schematically illustrated in Fig. 14. The characterization results above revealed the formation of defects in the catalyst due to the increase in the hydrothermal condition. As a result, the trap state energy levels are formed within the band-gap of TiO_{2-x}. The presence of the defects is known to strengthen the absorption in both UV and visible light regions. In addition, Ti^{3+} can act also as hole traps to suppress the recombination with the electron. In addition, the presence of glassy carbon helps in decreasing the charge carriers recombination,[17] leading to overall improved photocatalytic activity towards the phenol degradation.[46] On the other hand, the applicability of the Langmuir–Hinshelwood (L–H) model to the photodegradation results (see Fig. S3†) suggests the adsorption of phenol on the photocatalyst surface before being decomposed photocatalytically. Finally, the formed radicals react with the adsorbed phenol on the surface and degrade it.

The ultimate goal of synthesizing a magnetically recoverable photocatalyst is to reuse it several times. Thus, the two best formulations were used in photocatalytic phenol removal several times. The photocatalysts were recovered magnetically and then introduced in the next experiment. Fig. 15 shows the variation in the phenol removal efficiency from one experiment to another. The efficiency decreased after the second

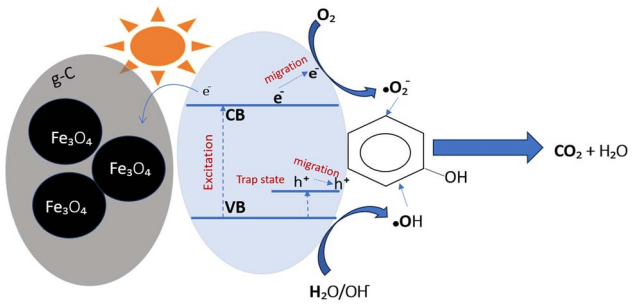

Fig. 14 Photocatalytic mechanism.

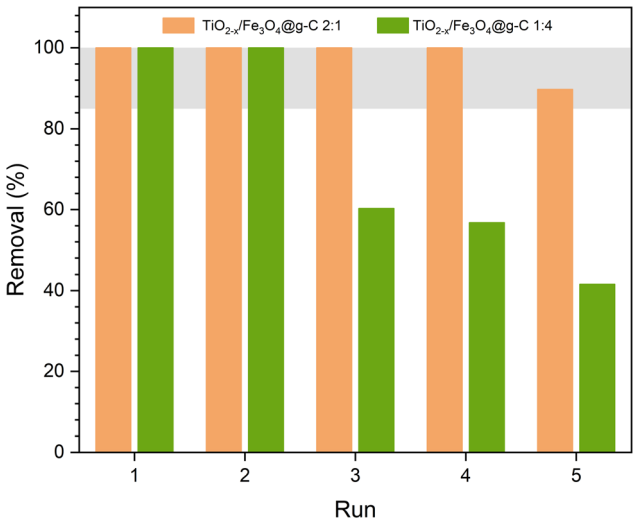

Fig. 15 Reusability of the best samples.

experiment when using the TiO_{2-x} : Fe_3O_4@g-C 1 : 4 composite. According to Fig. 13a, the rate of phenol degradation in this case is low, leading to the incomplete degradation of phenol within 4 h. In order to ensure that phenol was completely degraded, the reusability test was extended to 7 h. Although this duration was efficient for complete phenol degradation, it caused an accumulation of the formed by-product on the catalyst surface even after washing the catalyst with DW and ethanol. Overall, the removal percentage decreased from one run to the next. On the contrary, the TiO_{2-x} : Fe_3O_4@g-C 2 : 1 composite showed an excellent stable performance, revealing the stability of the composite. As its rate of degradation was high according to Fig. 13a, it caused the complete degradation of phenol in 4 h, making 7 h enough to degrade all the by-products and clean the catalyst surface.

4. Conclusion

Defective TiO_{2-x} was successfully prepared under different temperature and time conditions following a hydrothermal method. The formation of the anatase phase was demonstrated in the prepared samples. The formation of the defects was also confirmed. TiO_{2-x} 200 °C/12 h and TiO_{2-x} 200 °C/24 h samples showed a significant degree of defects; however, in case of TiO_{2-x} 200 °C/12 h, the formation of massive defects negatively affects its performance. On the other hand, TiO_{2-x} 200 °C/24 h showed the better removal of phenol. This could be attributed to the formation of defects and enhanced crystal growth that occurred on increasing the hydrothermal time. The defective composite TiO_{2-x}/Fe_3O_4@g-C 200 °C/24 h was successfully prepared. The formation of chemical bonding between the two components was revealed by XPS analysis. Setting the ratio between Fe_3O_4@g-C and TiO_{2-x} at 1 : 2 and 4 : 1 resulted in the best photocatalytic performance. However, the reusability test shows more degradation stability of the 1 : 2 ratio even after 5 runs.

Data availability

All data generated or analysed during this study are included in this article.

Conflicts of interest

There are no conflicts to declare.

Acknowledgements

This paper is based upon work supported by Science, Technology & Innovation Funding Authority (STDF) under grant number 37078.

References

1 (*a*) J. Zhang, F. Chen and B. He, *Photocatalysis*, Springer, 2018, DOI: 10.1007/978-981-13-2113-9; (*b*) D. V. Bavykin, J. M. Friedrich and F. C. Walsh, Protonated Titanates and TiO2 Nanostructured Materials: Synthesis, Properties, and Applications, *Adv. Mater.*, **18**(21), 2807–2824.

2 A. Fujishima and K. Honda, Electrochemical evidence for the mechanism of the primary stage of photosynthesis, *Bull. Chem. Soc. Jpn.*, 1971, **44**(4), 1148–1150.

3 T. Rajaraman, S. P. Parikh and V. G. Gandhi, Black TiO2: A review of its properties and conflicting trends, *Chem. Eng. J.*, 2020, **389**, 123918.

4 S. Mereym, S. Nasreen, M. Siddique and R. Khan, An overview of the reaction conditions for an efficient photoconversion of CO2, *Rev. Chem. Eng.*, 2017, **34**, 409–425.

5 S. C. Ameta and R. Ameta, *Advanced Oxidation Processes for Wastewater Treatment: Emerging Green Chemical Technology*, Academic Press, 2018.

6 J. Low, J. Yu, M. Jaroniec, S. Wageh and A. A. Al-Ghamdi, Heterojunction photocatalysts, *Adv. Mater.*, 2017, **29**(20), 1601694.

7 X. Ding, W. Ho, J. Shang and L. Zhang, Self doping promoted photocatalytic removal of no under visible light with bi2moo6: Indispensable role of superoxide ions, *Appl. Catal., B*, 2016, **182**, 316–325.

8 S. Na, S. Seo and H. Lee, Recent Developments of Advanced Ti3+-Self-Doped TiO2 for Efficient Visible-Light-Driven Photocatalysis, *Catalysts*, 2020, **10**(6), 679.

9 S. Bai, N. Zhang, C. Gao and Y. Xiong, Defect engineering in photocatalytic materials, *Nano Energy*, 2018, **53**, 296–336.
10 L. Yang, L. Xu, X. Bai and P. Jin, Enhanced visible-light activation of persulfate by Ti3+ self-doped TiO2/graphene nanocomposite for the rapid and efficient degradation of micropollutants in water, *J. Hazard. Mater.*, 2019, **365**, 107–117.
11 C. Wu, Z. Gao, S. Gao, Q. Wang, H. Xu, Z. Wang, *et al.*, Ti3+ self-doped TiO2 photoelectrodes for photoelectrochemical water splitting and photoelectrocatalytic pollutant degradation, *J. Energy Chem.*, 2016, **25**(4), 726–733.
12 H. Danan, A. Herr and A. Meyer, New determinations of the saturation magnetization of nickel and iron, *J. Appl. Phys.*, 1968, **39**(2), 669–670.
13 X. Wang, P. Zhang, W. Wang, X. Lei, B. Zou and H. Yang, Synthesis, structure and magnetic properties of graphite carbon encapsulated Fe 3 C nanoparticles for applications as adsorbents, *RSC Adv.*, 2015, **5**(35), 27857–27861.
14 M. D. Nguyen, H.-V. Tran, S. Xu and T. R. Lee, Fe3O4 nanoparticles: structures, synthesis, magnetic properties, surface functionalization, and emerging applications, *Appl. Sci.*, 2021, **11**(23), 11301.
15 S. Rajendran, A. Blanco, L. Gnanasekaran, A. A. Jalil, W.-H. Chen and F. Gracia, Harvesting visible light for enhanced catalytic degradation of wastewater using TiO2@Fe3O4 embedded on two dimensional reduced graphene oxide nanosheets, *Chemosphere*, 2023, **345**, 140418.
16 M. Nadimi, A. Ziarati Saravani, M. A. Aroon and A. Ebrahimian Pirbazari, Photodegradation of methylene blue by a ternary magnetic TiO2/Fe3O4/graphene oxide nanocomposite under visible light, *Mater. Chem. Phys.*, 2019, **225**, 464–474.
17 K. Jurkiewicz, M. Pawlyta, D. Zygadło, D. Chrobak, S. Duber, R. Wrzalik, *et al.*, Evolution of glassy carbon under heat treatment: correlation structure–mechanical properties, *J. Mater. Sci.*, 2018, **53**(5), 3509–3523.
18 V. Uvarov and I. Popov, Metrological characterization of X-ray diffraction methods at different acquisition geometries for determination of crystallite size in nano-scale materials, *Mater. Charact.*, 2013, **85**, 111–123.
19 M. F. B. M. Na'aim, R. M. B. Ramli and N. A. B. M. Zabidi, Synthesis of ascorbic acid enhanced TiO2 photocatalyst: its characterization and catalytic activity in CO2 photoreduction, *Metall. Mater. Eng.*, 2018, **24**(1), 1–16.
20 E. H. Mert, Y. Yalçın, M. Kılıç, N. San and Z. Çınar, Surface modification of TiO2 with ascorbic acid for heterogeneous photocatalysis: theory and experiment, *J. Adv. Oxid. Technol.*, 2008, **11**(2), 199–207.
21 P. Makuła, M. Pacia and W. Macyk, How To Correctly Determine the Band Gap Energy of Modified Semiconductor Photocatalysts Based on UV–Vis Spectra, *J. Phys. Chem. Lett.*, 2018, **9**(23), 6814–6817.
22 D. Li, H. Song, X. Meng, T. Shen, J. Sun, W. Han, *et al.*, Effects of Particle Size on the Structure and Photocatalytic Performance by Alkali-Treated TiO2, *Nanomaterials*, 2020, **10**(3), 546.
23 M. Wajid Shah, Y. Zhu, X. Fan, J. Zhao, Y. Li, S. Asim, *et al.*, Facile synthesis of defective TiO2− x nanocrystals with high surface area and tailoring bandgap for visible-light photocatalysis, *Sci. Rep.*, 2015, **5**(1), 1–8.
24 L. Han, B. Su, G. Liu, Z. Ma and X. An, Synthesis of oxygen vacancy-rich black TiO2 nanoparticles and the visible light photocatalytic performance, *Mol. Catal.*, 2018, **456**, 96–101.
25 T. Wang, W. Li, D. Xu, X. Wu, L. Cao and J. Meng, A novel and facile synthesis of black TiO_2 with improved visible-light photocatalytic H_2 generation: Impact of surface modification with CTAB on morphology, structure and property, *Appl. Surf. Sci.*, 2017, **426**, 325–332.
26 M. Gu, L. Pan, B. Tay and C. Q. Sun, Atomistic origin and temperature dependence of Raman optical redshift in nanostructures: a broken bond rule, *J. Raman Spectrosc.*, 2007, **38**(6), 780–788.
27 Z. Liang, J. Li, N. Lei, L. Guo and Q. Song, Construction of Ti 3+ self-doped TiO 2/BCN heterojunction with enhanced photoelectrochemical performance for water splitting, *J. Mater. Sci.: Mater. Electron.*, 2019, **30**, 2006–2015.
28 F. Meng, S. Zhang, X. Li, Y. Zeng and Q. Zhong, CrOx assembled at the oxygen vacancies on black-TiO2 for NO oxidation, *Mol. Catal.*, 2019, **473**, 110393.
29 D. Zhang, X. Ma, H. Zhang, Y. Liao and Q. Xiang, Enhanced photocatalytic hydrogen evolution activity of carbon and nitrogen self-doped TiO2 hollow sphere with the creation of oxygen vacancy and Ti3+, *Mater. Today Energy*, 2018, **10**, 132–140.
30 P. Wen, Y. Zhang, G. Xu, D. Ma, P. Qiu and X. Zhao, Ti3+ self-doped TiO2 as a photocatalyst for cyclohexane oxidation under visible light irradiation, *Journal of Materiomics*, 2019, **5**(4), 696–701.
31 D. Xue, J. Luo, Z. Li, Y. Yin and J. Shen, Enhanced photoelectrochemical properties from Mo-doped TiO2 nanotube arrays film, *Coatings*, 2020, **10**(1), 75.
32 T. A. Gad-Allah, R. Zhang, Y. Wang and Y. Zhou, Facile one-pot synthesis of defective (001)-TiO2− x/h-BN photocatalyst for environmental applications, *J. Alloys Compd.*, 2023, **954**, 170187.
33 M. Stefan, O. Pana, C. Leostean, C. Bele, D. Silipas, M. Senila, *et al.*, Synthesis and characterization of Fe3O4–TiO2 core-shell nanoparticles, *J. Appl. Phys.*, 2014, **116**(11), 114312.
34 J. Huo, Y. Hu, H. Jiang and C. Li, In situ surface hydrogenation synthesis of Ti 3+ self-doped TiO 2 with enhanced visible light photoactivity, *Nanoscale*, 2014, **6**(15), 9078–9084.
35 Z. Cai, Y. Bi, E. Hu, W. Liu, N. Dwarica, Y. Tian, *et al.*, Single-crystalline ultrathin Co3O4 nanosheets with massive vacancy defects for enhanced electrocatalysis, *Adv. Energy Mater.*, 2018, **8**(3), 1701694.
36 C. Jin, B. Liu, Z. Lei and J. Sun, Structure and photoluminescence of the TiO 2 films grown by atomic layer deposition using tetrakis-dimethylamino titanium and ozone, *Nanoscale Res. Lett.*, 2015, **10**, 1–9.
37 M. S. Abdel-Wahed, A. S. El-Kalliny, F. A. Shehata, A. M. Abd El-Aty and T. A. Gad-Allah, One-pot green synthesis of magnetic adsorbent via Anabaena sphaerica and its

performance towards Remazol Red dye removal from aqueous media, *Chem. Eng. Sci.*, 2023, 118939.

38 J. Chen, J. Li, D. Xiong, Y. He, Y. Ji and Y. Qin, Preparation and tribological behavior of Ni-graphene composite coating under room temperature, *Appl. Surf. Sci.*, 2016, **361**, 49–56.

39 E. Castagnola, S. Thongpang, M. Hirabayashi, G. Nava, S. Nimbalkar, T. Nguyen, *et al.*, Glassy carbon microelectrode arrays enable voltage-peak separated simultaneous detection of dopamine and serotonin using fast scan cyclic voltammetry, *Analyst*, 2021, **146**(12), 3955–3970.

40 U. Szeluga, S. Pusz, B. Kumanek, K. Olszowska, S. Czajkowska, J. Myalski, *et al.*, Influence of unique structure of glassy carbon on morphology and properties of its epoxy-based binary composites and hybrid composites with carbon nanotubes, *Compos. Sci. Technol.*, 2016, **134**, 72–80.

41 M. Frenea-Robin and J. Marchalot, Basic principles and recent advances in magnetic cell separation, *Magnetochemistry*, 2022, **8**(1), 11.

42 J. López, A. Rey, E. Viñuelas-Zahinos and P. M. Álvarez, Preparation of a new green magnetic Fe3O4 @TiO2-P25 photocatalyst for solar advanced oxidation processes in water, *J. Environ. Chem. Eng.*, 2023, **11**(3), 109999.

43 C. Fu, G. Zhao, H. Zhang and S. Li, A facile route to controllable synthesis of Fe3O4/graphene composites and their application in lithium-ion batteries, *Int. J. Electrochem. Sci.*, 2014, **9**(1), 46–60.

44 H. Wang, X. Xu and A. Neville, In situ synthesis of nanostructured Fe 3 O 4@ TiO 2 composite grown on activated carbon cloth as a binder-free electrode for high performance supercapacitors, *RSC Adv.*, 2021, **11**(38), 23541–23549.

45 U. Naknikham, G. Magnacca, A. Qiao, P. K. Kristensen, V. Boffa and Y. Yue, Phenol abatement by titanium dioxide photocatalysts: effect of the graphene oxide loading, *Nanomaterials*, 2019, **9**(7), 947.

46 G. K. Q. Ganharul, A. Tofanello, A. Bonadio, A. L. M. Freitas, M. T. Escote, A. S. Polo, *et al.*, Disclosing the hidden presence of Ti3+ ions in different TiO2 crystal structures synthesized at low temperature and photocatalytic evaluation by methylene blue photobleaching, *J. Mater. Res.*, 2021, **36**(16), 3353–3365.